JACS
JOURNAL OF THE AMERICAN CHEMICAL SOCIETY

Article

pubs.acs.org/JACS

Iodide-Mediated Control of Rhodium Epitaxial Growth on Well-Defined Noble Metal Nanocrystals: Synthesis, Characterization, and Structure-Dependent Catalytic Properties

Brian T. Sneed, Chun-Hong Kuo, Casey N. Brodsky, and Chia-Kuang Tsung*

Department of Chemistry, Merkert Chemistry Center, Boston College, 2609 Beacon Street, Chestnut Hill, Massachusetts 02467, United States

Supporting Information

ABSTRACT: Metal nanocrystals (NCs) comprising rhodium are heterogeneous catalysts for CO oxidation, NO reduction, hydrogenations, electro-oxidations, and hydroformylation reactions. It has been demonstrated that control of structure at the nanoscale can enhance the performance of a heterogeneous metal catalyst, such as Rh, but molecular-level control of NCs comprising this metal is less studied compared to gold, silver, platinum, and palladium. We report an iodide-mediated epitaxial overgrowth of Rh by using the surfaces of well-defined foreign metal crystals as substrates to direct the Rh surface structures. The epigrowth can be accomplished on different sizes, morphologies, and identities of metal substrates. The surface structures of the resulting bimetallic NCs were studied using electron microscopy, and their distinct catalytic behaviors were examined in CO stripping and the electro-oxidation of formic acid. Iodide was found to play a crucial role in the overgrowth mechanism. With the addition of iodide, the Rh epigrowth can even be achieved on gold substrates despite the rather large lattice mismatch of ~7%. Hollow Rh nanostructures have also been generated by selective etching of the core substrates. The new role of iodide in the overgrowth and the high level of control for Rh could hold the key to future nanoscale control of this important metal's architecture for use in heterogeneous catalysis.

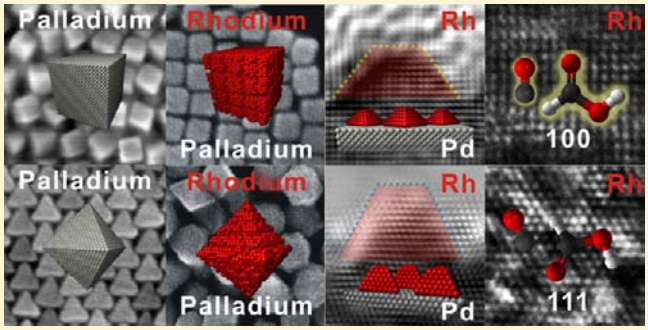

INTRODUCTION

The rational design of new generation heterogeneous catalysts with high performance requires control over their architecture at the nanoscale. The size and shape control of nanostructures determines their catalytic behavior through the adjustment of the number and geometric structure of the active sites. The nanoscale architectural control of the interface between metal−metal and metal−metal oxide[1−3] can be used to tune the electronic structure of the active sites.[4] Significant enhancement of transition-metal catalysts can be achieved by tuning the geometric and electronic structure because these characteristic properties determine the d-band center, which affects the sorption behavior of molecules on the surface of the metals. These structural controls have been less studied for systems comprising rhodium, while structures and methodologies for the synthesis and study of other noble metal nanocrystals (NCs) have been extensively developed.

Rh is a choice metal for this study not only because of the lack of structural control but also because of its versatility, activity, and selectivity over so many chemical transformations, such as NO reduction, CO oxidation, electro-oxidations, hydrogenations, and hydroformylations.[5−9] Controlling the size, shape, and composition of Rh overgrowth in a core−shell structure could allow for similar advancements in the metal's application toward enhanced heterogeneous catalysis, electrocatalysis, hydrogen storage, and plasmon-enhanced catalysis.[6−21] The lack of structural control for Rh could be attributed to the small number of suitable surfactants or adsorbate additives which can stabilize the growing Rh surface in such a way as to expose specific facets. Halide or pseudohalide anions have been extensively used as additives for shape control of Au, Pd, and Pt NCs,[22,23] but so far this strategy has not been successfully utilized with Rh nanoparticle synthetic methods.

Some pioneer examples of shape-controlled Rh particles have been displayed,[6,19,24−31] but roughness and particle irregularity remain problems to be overcome, and the surface facets have not been well studied. The formation of irregular dendritic particles and networks is commonly observed with Rh crystal growth.[18,32] This morphology has been reported using other noble metals such as Pt.[33] The strategy of introducing shaped metal seeds during the synthesis has been developed as an alternative route to achieve morphological control. The use of a structure-controlled crystal substrate to direct overgrowth has been reported as an effective method for control of the surface structure and metal−metal interface in bimetallic systems.[1,34,35] Nevertheless, the Rh overgrowth achieved by using this strategy is not well developed.

Received: August 16, 2012
Published: October 3, 2012

   dx.doi.org/10.1021/ja308030h | J. Am. Chem. Soc. 2012, 134, 18417−18426

In this study, we aim at using noble metal substrates to epitaxially grow highly ordered Rh nanoisland crystals with a controlled size, orientation, surface structure, and interface. These well-controlled model catalysts could be used to study overgrowth behaviors and structure-dependent catalysis of Rh. Scheme 1 illustrates how the monodisperse and shape-controlled NCs of Pd and Au were used as substrates to generate the Rh island epigrowth with the assistance of iodide adsorbate ions. Ascorbic acid was used as reducing agent in the aqueous cetyltrimethylammonium bromide (CTAB) solution (Scheme S1). The tunable size of the Rh overgrowth and the variety of sizes, metal types, and morphologies of the substrate NCs employed demonstrate that this is a general method which can offer a new level of control of Rh. Directing the Rh epigrowth at the atomic level on these metal substrate NCs could offer advantages to catalytic performance through both modification of the surface electronic and geometric structure and through the introduction of a controlled metal interface.[36−39] We demonstrate that the substrate NCs impart their morphology to the Rh growth which influences its activity toward CO stripping and formic acid oxidation electrocatalysis.

Scheme 1. Synthetic Strategy for Controlled Rh Epigrowth on Noble Metal NCs

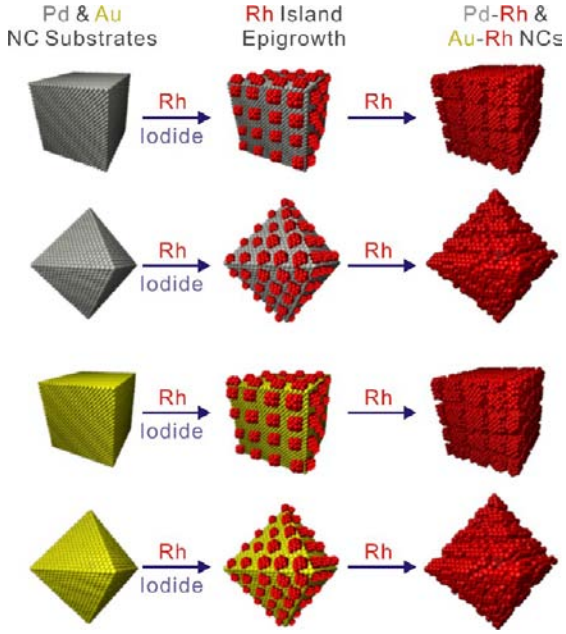

RESULTS AND DISCUSSION

Electron microscopy was used to characterize the NCs that were synthesized. Figure 1 displays the highly uniform Pd nanocubes and nanooctahedra synthesized and used as substrates for the overgrowth of Rh. The relatively large size of the shaped crystals (~30 and ~60 nm on edge for cubes and octahedra, respectively) allows us to systematically study the growth on different crystal facets, as their surface facets are well-defined in this size range. The overgrowth is observed to take on a grid-like arrangement of islands extending from the palladium surface. Rh's preference for island epitaxy is explained using bond dissociation and surface energies. Since the bond dissociation energy between atoms is higher with Rh, atoms prefer to deposit on preformed islands rather than on the Pd surface so that the interfacial strain between Pd and Rh is reduced. Since ascorbic acid is a weaker reducing agent, already deposited Rh will autocatalyze further reduction only at the surface of the growing islands.

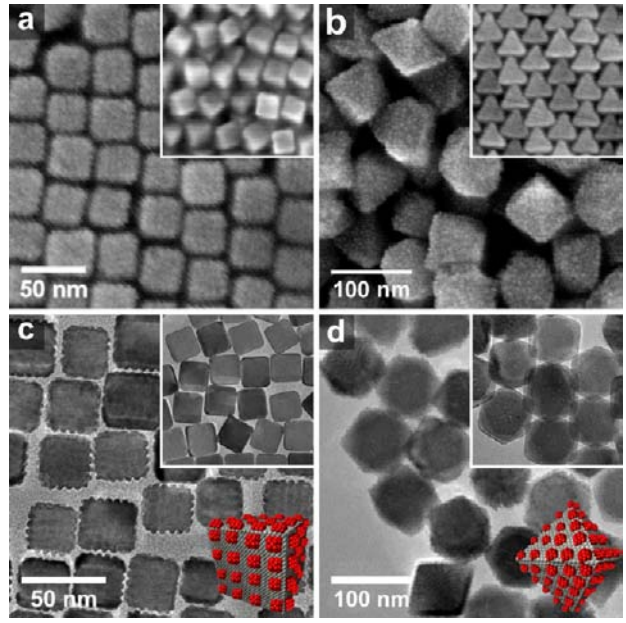

Figure 1. Electron microscope images. SEM (a,b) and TEM (c,d) images were taken for Pd nanocubes (a,c) and nanooctahedra (b,d) with Rh overgrowth. Insets show the corresponding uniform substrate crystals before the Rh overgrowth.

Rh overgrowth on Pd and Au NCs has been studied previously,[32,40] but closer inspection reveals important characteristics of our NCs that set it apart from previous examples. The Pd−Rh NCs retain the overall shape of their substrate, and the Rh islands are observed to take on a distinct shape themselves. The size distribution of islands is highly uniform and their appearance is identical across hundreds of observed NCs. The epitaxial, single-crystalline nature of the Pd−Rh NCs is revealed by selected area electron diffraction (SAED) and high-resolution TEM (HRTEM). The size of the overgrowth islands can be tuned by changing the amount of Rh added. To confirm the crystalline structure of the overgrowth islands, the HRTEM images in conjunction with SAED patterns were obtained for a higher amount of Rh overgrowth on the different Pd substrate morphologies. Figure 2 shows the respective TEM, SAED, and HRTEM images for a single (a−c) Pd cube, (d−f) Pd−Rh cubic NC, (h,i) Pd octahedron, and (j−l) Pd−Rh octahedral NC. Despite some branching structures with higher amounts of Rh, the growth was still found to be single crsystalline; that is, occurring epitaxially from the substrate rather than by particle attachment from the solution. Cubic NCs are viewed from the [100] zone axis, and octahedral NCs are viewed from the [111] zone axis in the images. The single diffraction patterns of the Pd−Rh NCs clearly reveal the single crystalline, epitaxial nature of the overgrowth. The *d*-spacings obtained from SAED patterns of the NCs with Rh epigrowth are smaller in comparison to those for the pure Pd crystals (Figure 2b,e,h,k) because of Rh's smaller lattice parameters (lattice mismatch of ~2%).

The HRTEM images further verify the epitaxy of Rh on Pd substrates. The square 2D lattice observed for cubic NCs is typical for the {100} planes of the *fcc* metals, as is the hexagonal

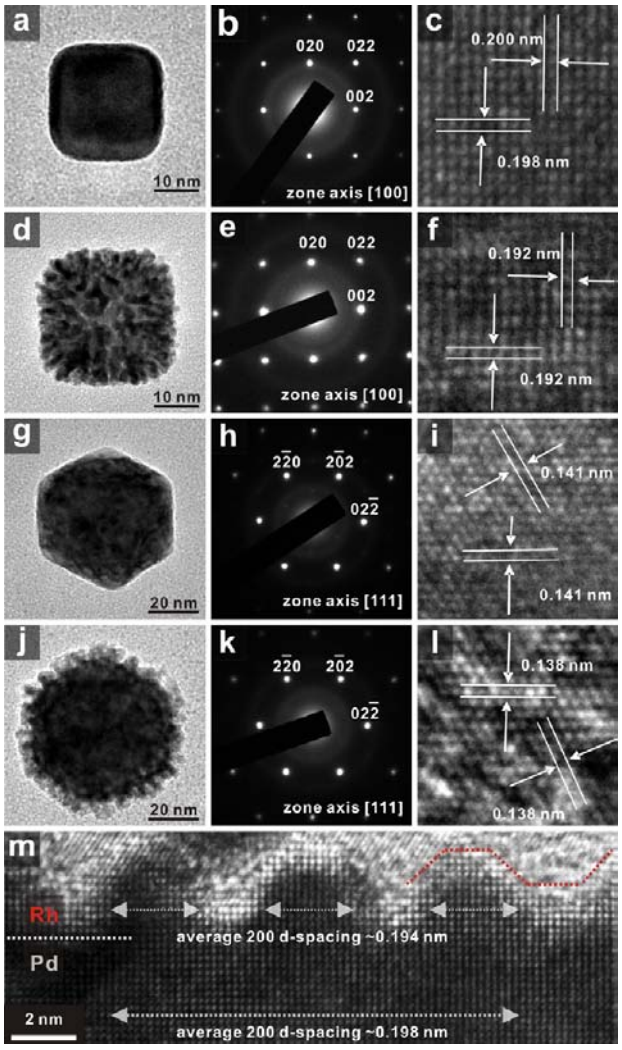

Figure 2. Structures of the Pd–Rd NCs. (a,d,g,j) TEM images, (b,e,h,k) SAED patterns, and (c,f,i,l) HRTEM images for rows (a–c) Pd cubic NC substrates, (d–f) Pd–Rh cubic NCs, (g–i) Pd octahedral NC substrates, and (j–l) Pd–Rh octahedral NCs. (m) HRTEM shows the different average *d*-spacings obtained for {200} planes at locations in the interface of Pd core and Rh island overgrowth.

lattice of the {111} planes observed for octahedral NCs. Note that for Pd–Rh lattice images (Figure 2f,l), the beam was focused on the Rh overgrowth portion of the NCs, where Rh *d*-spacings were measured. For cubic Pd substrates, *d*-spacings for the {200} planes were ~0.200 nm, and for the cubic Pd–Rh NCs, the *d*-spacing of {200} is 0.192 nm. For octahedral Pd substrates, the {220} *d*-spacing is 0.141 nm, while the Pd–Rh octahedral NC *d*-spacing is 0.138 nm. The *d*-spacings are in good agreement with those obtained for pure Pd and Rh from crystallographic databases for the respective metal's lattice planes (PCPDFWIN vs 2.02-International Centre for Diffraction Data, 1999). Figure 2m clearly displays the interface between Pd and Rh. Different average *d*-spacings are obtained for planes in the same direction but for different regions close to the interface (interior Pd cubic core and exterior Rh overgrowth). The average spacing is ~0.194 nm for the Rh overgrowth, whereas for the Pd core location, the spacing is 0.198 nm. The difference reveals the transition between the Pd and Rh metal phases. Hundreds of the Pd–Rh NCs were surveyed, but none could be found containing misaligned lattice fringes. This indicates all of the resulting island overgrowth is epitaxial. Particle formation and attachment from the solution have been observed with alternate methods for synthesizing Pd–Rh NCs, but this was not observed in our case.[32] The latter is significant as our method can generate Rh overgrowth with complete epitaxy and a higher degree of control over the island growth's uniformity in terms of both size and shape.

Powder X-ray diffraction (XRD) was performed to understand the overgrowth (Figures 3 and S1). The spectra for Pd–

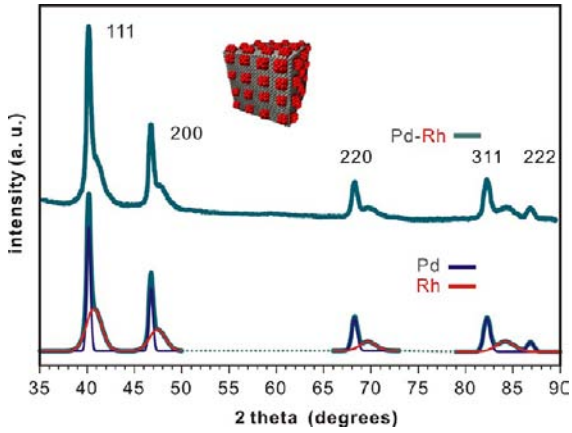

Figure 3. Powder XRD spectra for Pd–Rh NCs with 5 μmoles of Rh added for growth. The spectrum is deconvoluted to give the respective Pd and Rh contributions in the spectrum below.

Rh NCs show clear Pd diffraction patterns, which closely resemble that of the pure Pd NCs. A distinct Rh shoulder can be observed to the right of all of the Pd peaks. The centers of these shoulders lie at the expected position for Rh for all of the peaks. For example, the 111 peak max for Pd lies at ~40.2°, while the shoulder's center is at ~40.7°. The difference in the peak position for Pd and Rh is more pronounced at larger angles. Deconvolution of the spectrum reveals the contributions of Pd and Rh to the spectrum (Figure 3). The separation of the metallic phases indicates that the composition of the growth should be mainly pure Rh rather than Pd–Rh alloy. The broad Rh peaks are due to the smaller domain size relative to Pd. The crystal domain size calculated from the Rh deconvoluted peaks is ~6.0 nm, which is comparable to the average between the length and diameter of an individual Rh column.

Energy-dispersive X-ray (EDX) spectroscopy confirms the ability to control the metal ratio between the core and shell (Figure S2). The Pd substrate cores could be selectively etched away by diluted hydrochloric acid. The resulting hollow NCs retain their overall morphologies and well-aligned crystal domains, which indicates the islands are partially joined together. (Figure 4a–d). EDX spectroscopy shown in Figure 4e confirms that the Pd had been etched away and that the hollow NCs are composed of Rh. The corresponding spectrum of particles before etching is used for comparison above the spectrum for the hollow particles. There is disappearance of the signal for the Pd L-lines for hollow particles, and quantitatively no Pd could be detected. To the best of our knowledge, this is the first example of well-defined hollow Rh nanostructures, which will be investigated in future efforts as high surface area catalysts. It also demonstrates the ability to generate Rh NCs with more complex nanostructures with high surface area, stability, and defined morphology.[41]

dx.doi.org/10.1021/ja308030h | J. Am. Chem. Soc. 2012, 134, 18417–18426

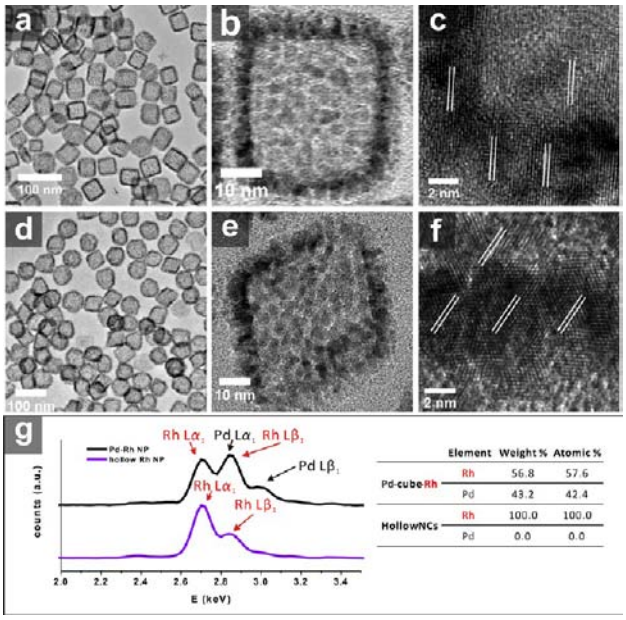

Figure 4. Hollow Rh NCs after selective etching of the Pd cores. TEM images of hollow (a–c) cubic and (d–f) octahedral Rh NCs. (g) EDX spectra of Pd–Rh NCs and the resulting hollow Rh NCs after etching.

The overgrowth progression was examined by changing the amount of Rh overgrowth on the Pd cubes shown in Figure 5. It was observed that the Rh overgrowth begins by reduction onto the Pd surface in the form of small islands (Figure 5a,d) at low concentration of Rh in the growth solution. These islands

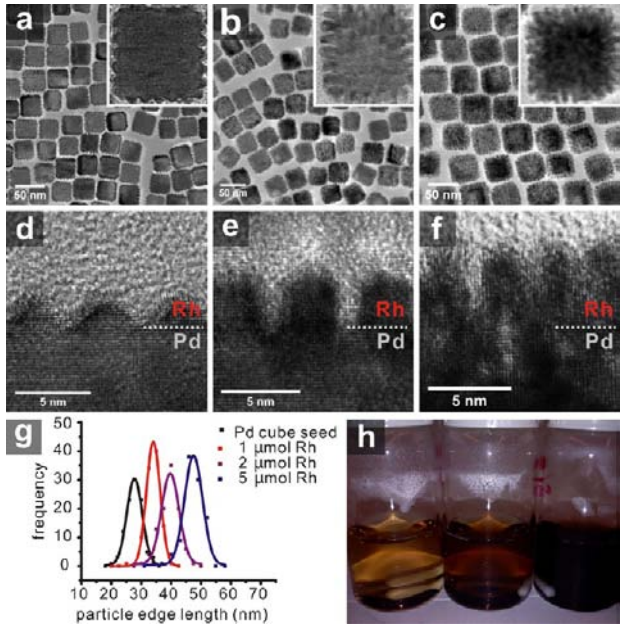

Figure 5. The overgrowth of Rh. TEM images of the Pd–Rh NCs are shown in with (a) 1, (b) 2, and (c) 5 μmol of Rh in the growth solution. Insets are high-magnification images of single particles. HRTEM images of the resulting Rh on Pd particles for each solution: (d) 1, (e) 2, and (f) 5 μmol of Rh in the growth solution. (g) Size distributions and a Gaussian fit are given in for the substrates and bimetallic particles (100 individual particle measurements per sample) as well as a (h) photo of each of the growth solutions postsynthesis (1, 2, and 5 μmol of Rh left to right).

are ~3 nm in diameter and arrange on the cube faces in grid-like patterns. A small amount of Pd surface may still be exposed. Subsequent growth appears to have preference for these just-formed islands, rather than filling spaces in between (Figure 5b,e). This type of growth mode (Volmer–Weber island growth)[42,43] has been observed previously with the noble metals.[1,32,33,44] Further growth of the islands produces small Rh columns of similar diameter to the islands extending from the Pd cores. Additional growth, shown in Figure 5c,f, results in a dense 'forest' of single-crystal Rh columns. The overgrowth can be tuned by the addition of Rh to give ~2–3 nm islands, ~5–6 nm columns, and ~8–10 nm long single-crystal columns of Rh (Figure 5g). The structure is open with channels observed between the columns. The overgrowth still retains the original crystal lattice orientation at even higher amounts of Rh because of the epitaxial overgrowth for the *fcc* metal. Though a limit for the overgrowth was not observed, small free Rh particles start to form in solution with higher precursor amounts, but the growth on substrates remains single crystalline. This information gives insight into the mechanism of growth observed and demonstrates our ability to control the overgrowth thickness by simply increasing or decreasing the amount of Rh in the growth solution.

The surface structures of the Rh islands were studied by HRTEM and electrochemistry. It was observed that the islands grown at lower Rh amounts appear to take on a specific, truncated pyramidal shape (Figure 6). Different structures for the Rh islands were proposed by comparing the HRTEM images and the crystal models. In the case where the Pd substrates are cubic, a majority of these Rh truncated pyramids should expose {100} facets at the upmost surfaces and a combination of {111}, {100}, and {110} facets on the sides of the islands. It is difficult to rule out the possibility of a small degree of high-index facets. A model and images for the cubic Pd–Rh islands are shown in Figure 6a–c. An angle of ~45° can be measured between the 100 direction (normal to the Pd cube surface) and the side of the pyramidal shaped islands. The normal to this plane should be the 110 direction based on the angle measurement. From this cross-section, we might conclude a 110 side surface or a 110 edge formed by two 111 planes (Figure 6c). The latter is more ideal since the 111 surface is more thermodynamically stable than 110. A similar shape for Rh islands was observed by P. Nolte et al.[45] They described a truncated Rh pyramid formed on a metal oxide substrate which was terminated by {100} and {111} surfaces. For the Pd substrates that are octahedral, a majority of the Rh pyramids likely expose {111} facets (Figures 6g–i), although again there is the likelihood for the presence of others. The angles measured from the cross-section lead us to believe that they are truncated tetrahedrons completely enclosed by {111} surfaces. The two distinct angles, ~35° and ~20°, measured between the side surface against the direction normal to the substrate surface correspond to the angles between a 100 edge (formed by two 111 planes) and a 111 plane, measured respectively, with the 111 direction. The proposed structures in the model shown in Figure 6i should give the observed lattice cross-section from the HRTEM images. Given this structural information, we speculate that the cubic NCs are dominantly enclosed by both {100} and {111} Rh facets, while there should be a majority of {111} Rh facets on the octahedral NCs. Furthermore, the difference between the two shapes is more distinguishable at higher amounts of overgrowth because the cubic NCs are dominantly enclosed by mainly {100} (Figures

dx.doi.org/10.1021/ja308030h | J. Am. Chem. Soc. 2012, 134, 18417–18426

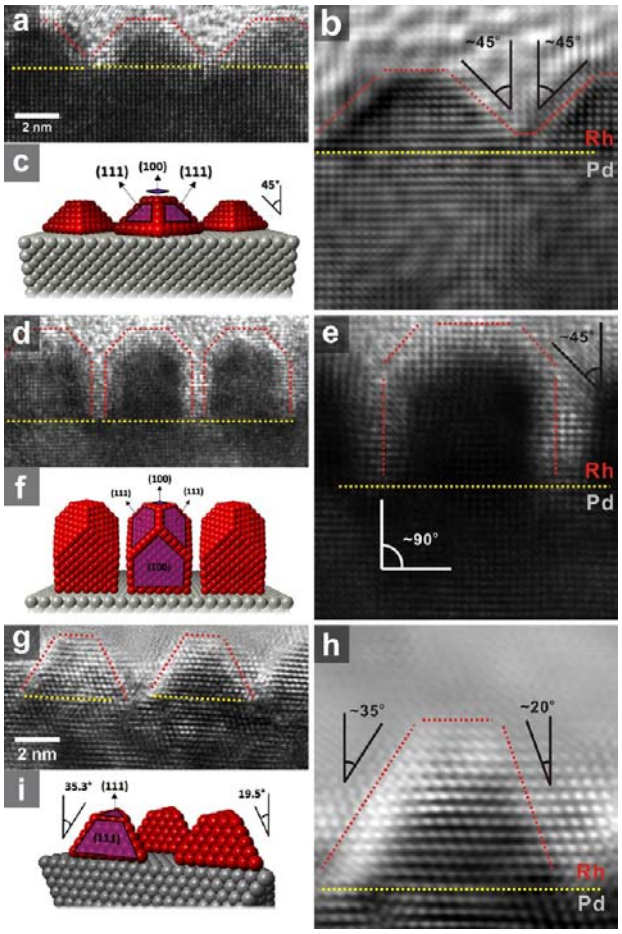

Figure 6. Surface structures of the Rh overgrowth. (a,d,g) HRTEM images, (b,e,h) FFT-enhanced images, (c,f,i) crystal models for (a–c) island overgrowth on Pd nanocubes, (d–f) column growth on Pd nanocubes, and (g–i) island growth on nanooctahedra.

6d–f and S6). The images in Figure 6d–f show how more overgrowth on cubic substrates generate more {100} surfaces due to the lengthening of islands into columns which should introduce sides that expose {100} facets. This conjecture is verified upon examination of the distinct electrocatalytic properties of the two Pd–Rh NCs with different morphologies. The results of this study are discussed below.

Electrocatalysis can be used as a powerful tool to probe the surface structure of metal NCs.[46] Many electrochemical reactions, including CO stripping and formic acid oxidation, are surface-structure sensitive, meaning both the potential required for the reaction and the current produced in the reaction depend on the surface structure of the catalyst. As a result, these reactions can be used to determine or confirm characteristics about the surface structure of metal NCs. Here, CO and formic acid oxidations were performed on the Pd–Rh NCs to investigate the surface structures. CO oxidation or "CO-stripping" occurs when a positive potential scan is applied to oxidize a monolayer of CO present on the surface of the metal NCs, yielding a characteristic peak for specific crystal facets of metal NCs. CO and OH adsorb on the surface of the metal and then react via a Langmuir–Hinshelwood reaction:[46]

$$CO_{ads} + OH_{ads} \rightarrow CO_2 + H^+ + e^- + 2*$$

where * indicates a free metal site.

Based on this mechanism, CO stripping is more favorable on Rh surfaces with more open crystal facets, which have lower-coordinated metal atoms. Thus the {100} crystal facet requires less energy to catalyze CO stripping than the {111} facet, and the CO stripping peak occurs at a lower potential on the {100} facet than the {111}.[47,48] CO-stripping experiments were performed using cubic and octahedral Pd–Rh NCs with 5 μmol of Rh overgrowth (large Rh columns), after running 50 blank scans in sulfuric acid. The resulting voltammograms are shown in Figure 7a. The cubic NCs exhibit a CO-stripping peak at a

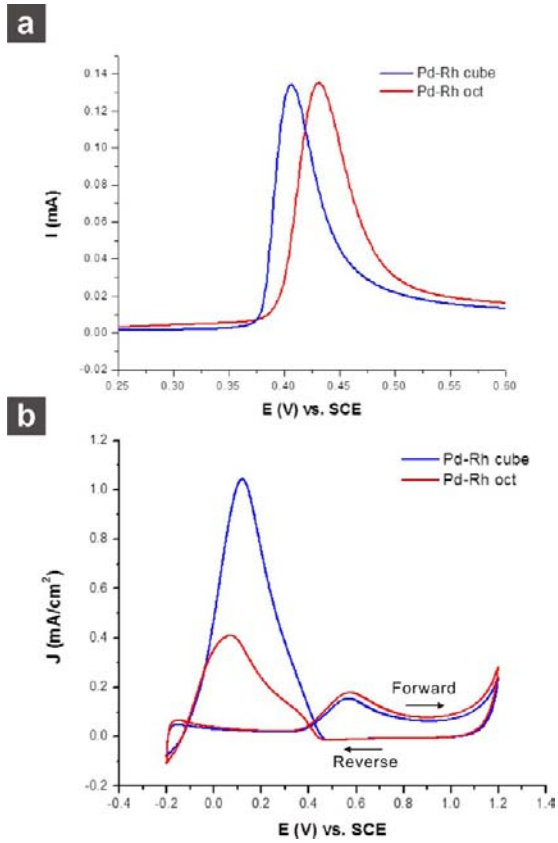

Figure 7. Cyclic voltammetry curves obtained for (a) CO stripping and (b) formic acid electro-oxidation. Integration of the CO-stripping current was used to calculate the electrochemically active surface area to normalize the activity of the catalysts for formic acid oxidation.

lower potential than the octahedral NCs. The CO-stripping experiment, therefore, confirms that the surfaces of synthesized Pd–Rh cubic NCs are different from that of Pd–Rh octahedral NCs. The difference could be mainly attributed to the {100} crystal facets at the surface of the cubes and the {111} crystal facets at the surface of the octahedra. This is in good agreement with our finding that the Rh overgrowth has a certain degree of facet control imparted by the structures of the crystal substrates. It is important to note that some of the surface Rh atoms can be oxidized at a relatively low potential (0.5–0.7 V vs RHE, depending on the facet).[47] The repeated oxidation and reduction of surface Rh atoms results in the formation of defect sites distributed evenly over the surface. As CO oxidation takes place preferentially at defect sites, this surface roughening step increases the particles' catalytic activity. Because the surface structure of the cubic Pd–Rh NCs is different from that of the octahedral Pd–Rh NCs, the morphologies exhibit

dx.doi.org/10.1021/ja308030h | J. Am. Chem. Soc. 2012, 134, 18417–18426

characteristic CO stripping peak potentials, even after surface roughening.

Formic acid oxidation experiments were also carried out for both cubic and octahedral Pd−Rh NCs with 5 μmol of Rh overgrowth, and the voltammograms are shown in Figure 7b. For both morphologies, the voltammogram exhibits two peaks, one near 0.1 V and one near 0.6 V. This two-peak graph is characteristic of an indirect formic acid oxidation pathway, in which the mechanism involves a CO-poisoning intermediate:[46]

$$HCOOH \rightarrow CO + H_2O \rightarrow CO_2 + 2H^+ + 2e^-$$

It is known that formic acid oxidation follows an indirect pathway on Rh,[49] whereas it follows a direct pathway through an adsorbed formate intermediate on Pd.[50] According to the obtained voltammograms, the synthesized Rh−Pd NCs are indeed enclosed by Rh surfaces as the curves do not follow a direct pathway. The main formic acid oxidation peak, in which CO is oxidized to CO_2, near 0.1 V, occurs at a similar potential for both the cubic and octahedral NCs. The current density (normalized by electrochemically active surface area) for the cubic NCs is approximately twice the current density for the octahedral NCs, showing that the cubic NCs have a higher intrinsic activity for formic acid oxidation than the octahedral NCs. It has been reported previously that the {100} crystal facet is more active than the {111} for formic acid oxidation on a Pt surface, because formic acid oxidation takes place preferentially on more open metal surfaces.[51] As it is known that formic acid oxidation follows the same mechanism on Rh as on Pt,[49] it is probable that Rh follows the same trend in crystal facet activity. We have shown that our Pd−Rh cubic NCs have a more open surface than the octahedral NCs, and the formic acid oxidation experiment confirms this expected trend.

Upon investigation of how the method presented could generate more control for Rh, we found that iodide ions play the most important role in the overgrowth. Figure 8 displays TEM images and a photo which reveal that Rh overgrowth occurs in a much higher yield when the growth solution contains iodide ions. Figure 8a shows the overgrowth without any iodide ions, while Figure 8b shows those with iodide ions. (The irregularity of the Pd substrate particles used for overgrowth is due to their synthesis without the use of iodide in order to control the I-amount in the growth solution. The high yield of uniform cubic substrates shown previously was achieved by adding iodide ions.) A stark contrast is observed regarding the amount of Rh overgrowth with and without iodide ions. With the same amount of precursor, substrate NCs, and otherwise identical conditions, only solutions with iodide yielded significant overgrowth. The photo in Figure 8c is for solutions with and without I^- (right and left, respectively). The difference in the darkness of the solution confirms what is seen under TEM. The much darker solutions contain larger particles from more Rh overgrowth. The transformation or darkening of the growth solution is more rapid for the growth solutions which contain iodide. The color change for iodide solutions occurs in ∼2 min, while a more gradual slight darkening is observed for solutions without iodide. For solutions without iodide, a small amount of nanoparticles <1 nm were observed under TEM and are likely small Rh NCs that have formed in solution away from the substrate surface. This is evidence of the importance of iodide ions in the incorporation of Rh onto the Pd substrate surface. The critical roles of iodide ions are proposed and discussed here.

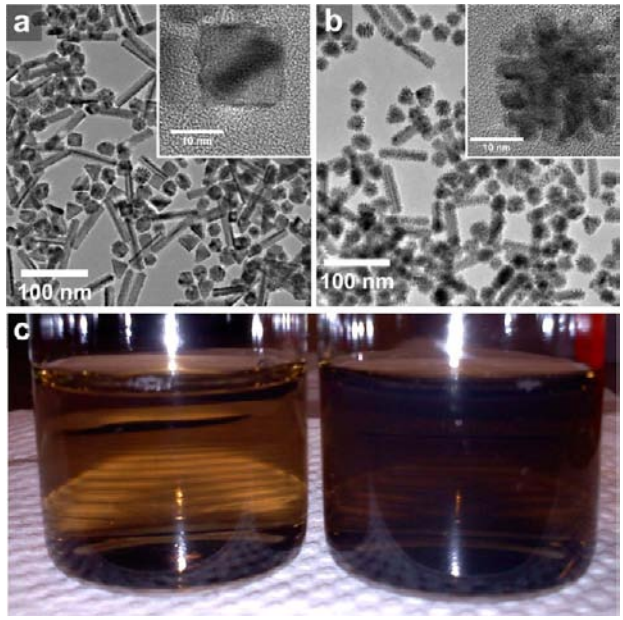

Figure 8. The critical role of iodide in the epitaxial overgrowth. Low-magnification TEM and HRTEM (insets) images of particles obtained (a) without and (b) with iodide in the growth solutions for intermediate amounts of Rh (2 μmol). A different degree of color change can be seen in (c); a photo of growth solutions without iodide (left) and with iodide (right) for comparison.

Iodide ions may serve multiple functions to facilitate the epitaxial overgrowth. First, iodide ions decrease the reduction potential of the Rh ions by complexation, which decreases the formation of free Rh nuclei. Second, the iodide ions draw the Rh ions to the surfaces of substrate crystals due to their strong interaction with Pd. The Pd surfaces lower the barrier of reduction by introducing a substrate as a seed for the growth. Others have similarly invoked anion coordination as a powerful tool in drawing the precursor metal ions nearer to the seed crystal surface to accelerate the growth process.[52] Third, iodide itself could serve as a reducing or oxidizing agent as the I^-/I_2 red/ox pair, which would activate the Pd surface for Rh overgrowth.[53,54] Overall, the iodide ions inhibit the free nucleation of Rh in the solution, draw the Rh ions to the Pd surfaces, and promote the Rh reduction on the Pd surface.

In order to support this hypothesis and demonstrate the versatility of this method, smaller Pd cubes as well as Au octahedra and Au cubes were used as substrates for overgrowth (Figures 9 and 10). Iodide ions were added to promote the Rh overgrowth. The size of the Rh islands and columns remains ∼3 nm in width, regardless of crystal seed size and type. Using a Au substrate, a similar type of growth can be seen. Epitaxy was observed for the Au particles as well, despite the rather large lattice mismatch of ∼7%, compared to ∼2% for Pd−Rh. Observation of cubic Au−Rh NCs under TEM displays the Rh epigrowth also occurs on Au cubes under similar conditions.

Figure 10 shows overgrowth on Au cubes with 1, 2, and 5 μmol Rh in the growth solution. The same trend in epitaxial growth progression (island growth into columns) is observed in TEM and under HRTEM in Figure 10d despite the large lattice mismatch (∼7%). A photo of the respective growth solutions in Figure 10e displays the effect of Rh overgrowth on the Au core's visible surface plasmon resonance (SPR) band. The nanoparticle solutions become progressively bluer in appearance as more Rh is added to the substrate surface, because of

dx.doi.org/10.1021/ja308030h | J. Am. Chem. Soc. 2012, 134, 18417−18426

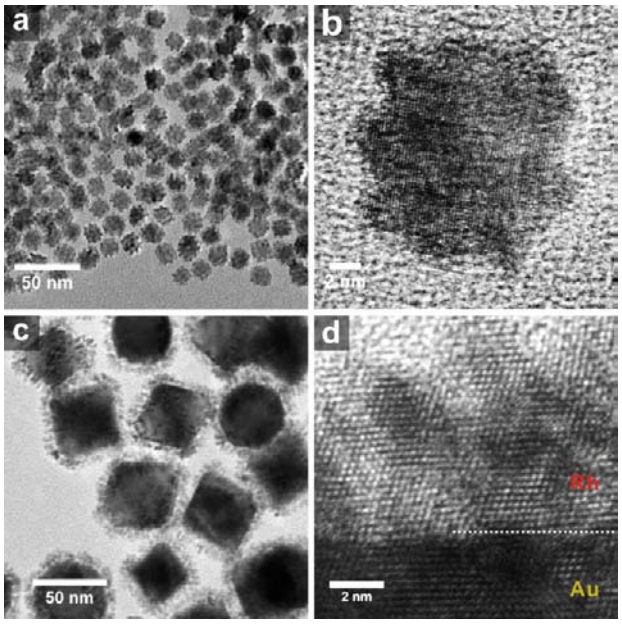

Figure 9. (a,c) TEM and (b,d) HRTEM images are shown for Rh overgrowth after changing the size, shape, and metal type of the substrates. For comparison, (a,b) 12 nm Pd cubes and (c,d) 60 nm Au octahedra were used.

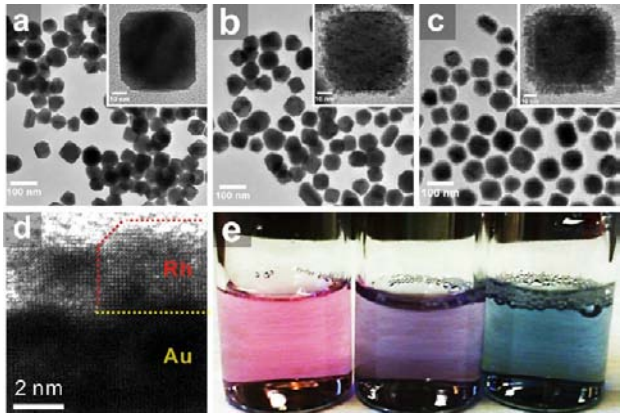

Figure 10. (a–c)TEM images of Rh overgrowth on Au nanocubes with increasing Rh amounts of (a) 1, (b) 2, and (c) 5 μmol Rh. (d) HRTEM of a selected particle shows the epitaxy between phases. (e) Photo of each of the solutions showing the effect of overgrowth on the SPR of the Au–Rh NCs.

the absorption and scattering due to the SPR. The effect of Rh overgrowth on the SPR band of the Au substrates was investigated using UV–vis spectroscopy. Extinction spectra shown in Figure 11a,c were obtained for cubic Au–Rh NCs with serial amounts of Rh in the growth solutions. A red-shift of the absorbance peak at ~530 nm is observed for the larger amounts of Rh precursor added to the solution. This peak not only shifts but also broadens after more overgrowth, demonstrating the effect of additional Rh epigrowth on the surface plasmon resonance of Au NCs. Quite recently, H. Chen et al. used Au–Pd overgrowth to elucidate the cause for this shift.[55] They have shown that the shift is due to percolation of the plasmon as the inhomogeneous growth perturbs the transition of the dielectric to the metal. In our system, we observe the same peak shift and broadening as what would be expected for a noncontinuous overgrowth. In this way we

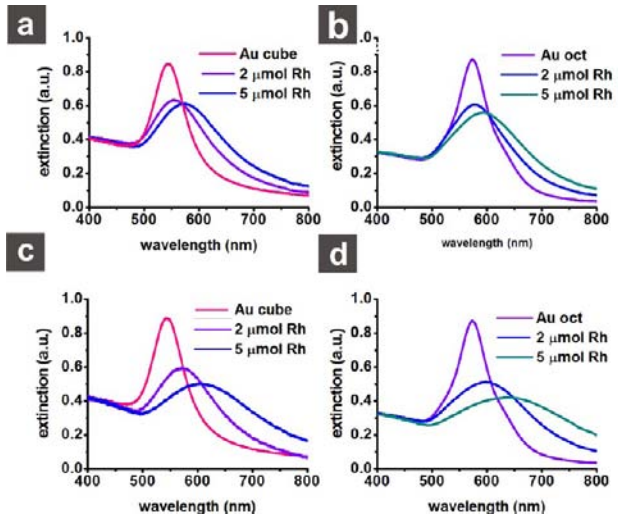

Figure 11. UV–vis spectra for cubic and octahedral Au–Rh nanoparticle solutions with different amounts of Rh overgrowth: (a) cubic and (b) octahedral nanoparticles synthesized without iodide in the growth solution for 0, 2, and 5 μmol of Rh in the growth solution. Extinction spectra for (c) cubic and (d) octahedral nanoparticles, respectively, synthesized with iodide added to the growth solution.

monitor the overgrowth of Rh on Au. Figure 11 clearly demonstrates the difference between the overgrowth with and without iodide ions. Solutions containing iodide (larger Rh overgrowth) show a much more dramatic shift in the SPR band. The Au–Rh nanostructures that can be generated by this method could offer great potential toward plasmonic catalysis.[21]

■ CONCLUSION

A novel method for synthesizing controlled Rh overgrowth on metallic NC substrates has been developed. Iodide in conjunction with a shape-controlled NC substrate directs the epitaxial overgrowth of Rh, which results in the formation of single-crystalline island shells. The new role of iodide in the overgrowth is unprecedented in the literature. The observed epitaxy in the case of Rh is accomplished here despite large lattice mismatches (~7% for Au–Rh), higher bond dissociation energies in the shell metal (Pd–Rh, Au–Rh), and higher electronegativity in the shell metal (Pd–Rh). The distinct surfaces were studied and confirmed by HRTEM and electrocatalysis. The model catalysts synthesized here might not be practical as industrial catalysts due to the relatively large size; however, we provide a powerful new tool for the high-level control of metal nanostructures, which could enrich the fundamental understanding of structure-dependent heterogeneous catalysis.

■ METHODS

Chemicals and Materials. Sodium iodide (NaI, 99.5%), potassium iodide (KI, 99.5%), sodium bromide (NaBr, 99%), L-ascorbic acid (99%), hydrochloric acid (HCl, 37%), palladium (II) chloride ($PdCl_2$, 99%), gold (III) chloride trihydrate ($AuCl_3 \cdot 3H_2O$, ~50% Au by wt.), rhodium (III) chloride hydrate ($RhCl_3 \cdot nH_2O$, ~40% Rh by wt.), hydroxylamine hydrochloride (NH_2OHHCl, 98%), perchloric acid ($HClO_4$, 70%), copper(II) chloride ($CuCl_2$, 97%), and formic acid (HCOOH, 95%) were all obtained from Sigma-Alrich. Cetyltrimethylammonium bromide (CTAB, 98%) was obtained from Calbiochem. Cetyltrimethylammonium chloride (CTAC, 99%) and sodium borohydride ($NaBH_4$, 99%) were obtained from Fluka. Sulfuric acid (H_2SO_4, 95%) and sodium hydroxide (NaOH, 95%)

dx.doi.org/10.1021/ja308030h | J. Am. Chem. Soc. 2012, 134, 18417–18426

were obtained from BDH. Carbon monoxide and nitrogen gas were obtained from Airgas. Deionized water (18.2 MΩ) was used in all procedures. Hydrochloric acid was used to prepare the acidic precursors for Au and Pd. Concentrated HCl was diluted, added to a beaker containing the metal chloride salt, and stirred under gentle heating to produce the 0.01 M stock solutions. Rhodium(III) chloride hydrate was dissolved and diluted in deionized water to obtain the precursor stock solution of 0.01 M $RhCl_3$.

Characterization. Samples were prepared for TEM and EDX spectroscopy by washing several times with DI water and placing 1.0 μL droplets of particle solutions on carbon-coated copper grids, which were then allowed to dry open to the air. The instrument used for both TEM and EDX was a JEOL JEM2010F accompanied by an EDX attachment operated at 200 kV. SEM was performed using a JEOL JSM6340F. Samples were prepared by placing a 1.0 μL droplet on a silicon wafer and allowing it to dry. The samples were then placed on silver glue atop double-sided copper tape on the sample holder. A Bruker AXS diffractometer was used to obtain the powder XRD patterns. Samples for XRD were prepared by placing 10 μL aliquots of concentrated nanoparticle solution on a glass slide and allowing them to dry in air. The diffraction database structure identification numbers (for the *fcc d*-spacings) for Au, Pd, and Rh are 04-0784, 87-0645, and 87-07148, respectively. The UV−vis extinction spectroscopy was obtained for diluted nanoparticle solutions using an Ocean Optics ISS UV−vis spectrometer.

Procedures. Pd NCs were synthesized via modification of a procedure from the literature.[22] Au NCs were also prepared from methods adapted from the literature.[56,57]

Synthesis of 30 nm Cubic Pd NC Substrates. A vial containing CTAB (0.05 g) and 9.300 mL of deionized water was sonicated until the CTAB was completely dissolved. Pd precursor (0.500 mL of 0.01 M H_2PdCl_4) was added to the solution, and a bright orange color was produced indicating the formation of the precursor complex with CTAB. The solution was then mixed, and 0.200 mL of 0.1 M NaI was added to the solution. The modification to the procedure improves the yield and uniformity of cubes. A color change from bright-orange to a dark-red color was observed after iodide addition. The solution was then heated for 5 min at 95 °C with gentle stirring, after which 0.200 mL of 0.04 M ascorbic acid was added to the vial. The solution was left to heat for an additional 30 min at 95 °C with stirring until the dark-red color was completely replaced by a dark-brown color, which indicated the completed formation of the NC substrates. The solution was removed from heat, allowed to cool, and then transferred to a 50 mL centrifuge tube and centrifuged for 15 min at 8000 rpm. The clear supernatant was decanted and discarded to yield a concentrated solution of Pd nanocubes. Seven reactions were repeated in the same fashion for a total of eight reaction solutions. The precipitated fractions were combined and redispersed with deionized water to a final volume of 10 mL resulting in a dark-brown colored solution (~4 mM in Pd), which was stored at room temperature for future use.

Synthesis of 60 nm Octahedral Pd NCs. A vial containing CTAB (0.3645 g) and 10 mL of deionized water was sonicated until the CTAB was completely dissolved. Pd precursor solution was added (0.250 mL of 0.01 M H_2PdCl_4) before adding 0.050 mL of 1 mM iodide reagent to the solution (results were identical whether using sodium or potassium cation in the iodide salt). This solution was heated for 5 min at 30 °C with stirring, after which 0.080 mL of previously prepared ~30 nm Pd cubes seed solution was added (prepared as described before, except that 300 μL of 0.01 M iodide was added), followed by 0.100 mL of 0.1 M ascorbic acid. The solution was then heated for 40 h at 30 °C with stirring. The solution was removed to cool, then transferred to a 50 mL centrifuge tube, and centrifuged for 15 min at 7000 rpm. The clear supernatant was decanted and discarded to yield a concentrated solution of Pd nanooctahedra. Eight of these reactions were also combined and redispersed with deionized water to a final volume of 5 mL of the dark-brown colored solution and stored at room temperature for later use (~4 mM in Pd).

Synthesis of 60 nm Octahedral Au NCs. CTAB (0.55 g) was combined with 97 mL of deionized water in a 250 mL beaker and sonicated to dissolve the white powder completely. The solution was then poured into a 200 mL pressure vessel (pressure vessels were obtained from ChemGlass), where to it was added 2.500 mL of 0.01 M $HAuCl_4$ (Au metal acidic precursor) and 0.400 mL of 0.1 M sodium citrate as the reducing agent. The resulting yellow-orange solution in the pressure vessel was swirled and sealed before being heated in an oven for 48 h at 110 °C. After this time the solution was removed from heat, allowed to cool, and centrifuged at 6000 rpm to give a clear supernatant and purple Au octahedral NC precipitate. The supernatant was decanted, and the NCs were redispersed in 6 mL of DI water for later use as seeds (~4 mM in Au).

Synthesis of 50 nm Cubic Au NCs. The procedure from the literature was followed accordingly to prepare the substrates. A 10 mL solution of 0.02 M $NaBH_4$ was first prepared and placed in an ice bath for future use. Then 0.03 g of CTAC, 9.3 mL of deionized water, and 0.25 mL of 0.01 M $HAuCl_4$ were combined together in a 20 mL scintillation vial. A stir bar was added, and the vial was placed on a stir plate. The stir rate was increased until a vortex was produced in the solution. Then 0.45 mL of the chilled borohydride solution was added to the solution at vortex producing a brownish-orange color. The solution was left at room temperature with stirring for 1 h to evolve off any unreacted borohydride. While the seed solution was left to stir, two growth solutions were made each containing 0.32 g CTAC, 9.625 mL of deionized water, 0.25 mL of the 0.01 M Au precursor solution, 0.01 mL of 0.01 M NaBr, and 0.09 mL 0.04 M ascorbic acid (added in this order; ascorbic acid was added just before the next step to give color change from yellow to a clear solution). A 0.025 mL aliquot of the seed solution was quickly added to one of the two growth solutions. After ~1 s the solution appeared just slightly pink. Immediately after viewing the beginning of the color change, a 0.025 mL aliquot was removed from the slightly pink solution and injected into the second growth solution. This solution was then mixed quickly and allowed to sit at 25 °C without agitation for 15 min. The cranberry colored solution was then centrifuged at 5000 rpm to yield cubic Au NCs ~50 nm on edge. A total of eight reactions were carried out in this manner, and their precipitated fractions were collected and concentrated in 5 mL to give a solution of ~4 mM in Au.

Synthesis of 12 nm Cubic Pd NC Substrates. A vial containing 0.05 g of CTAB and 9.300 mL of deionized water was sonicated until the CTAB was completely dissolved. A volume of 0.250 mL of 0.01 M H_2PdCl_4 was added to the solution. The vial was placed on a stir plate at room temperature and stirred until a vortex was established. Then 0.45 mL of 0.02 M $NaBH_4$ (previously prepared and put in an ice bath) was added, and a color change was observed indicating the reduction of Pd precursor. The reaction proceeded at room temperature for 1 h, after which the vial was removed from the stir plate. The solution containing small Pd seeds was set aside. A separate vial containing 0.05 g of CTAB and 9.300 mL of deionized water was sonicated until the CTAB was completely dissolved. A 0.500 mL amount of 0.01 M H_2PdCl_4 and 0.050 mL of 0.1 M sodium iodide was added to the solution. This solution was heated for 5 min at 60 °C with stirring, after which 0.050 mL of the seed solution and 0.100 mL of 0.04 M ascorbic acid were added to the vial. The solution was then heated for an additional 2 h at 60 °C with stirring. After the reaction, the solution was removed to cool, and then transferred to a 50 mL centrifuge tube, and centrifuged for 15 min at 14 000 rpm. The clear supernatant was decanted and discarded to yield a concentrated solution of Pd nanocubes. Eight of these reactions were concentrated, combined, and redispersed with deionized water to a final volume of 10 mL (~4 mM Pd) and stored at room temperature for later use as seeds for growth.

Synthesis of Rh Bimetallic NCs. Three vials containing 0.05g of CTAB and 9.3 mL of deionized water were sonicated until the CTAB was completely dissolved. Serial amounts of the Rh precursor (1, 2, and 5 μmoles of $RhCl_3$) were added to the solutions to obtain the respective thickness of Rh overgrowth, and 0.500 mL of the previously prepared seed solutions containing ~30 nm Pd cubes, ~12 nm Pd cubes, ~60 nm Pd octahedra, ~30 nm Au cubes, or ~60 nm Au octahedra were added to the solution, depending on the desired core metal/structure type (for solutions other than those containing ~30

nm Pd cubic seeds, 0.025 mL of 0.01 M sodium iodide was added to the solution after this step to promote the Rh overgrowth). The solutions were heated for 5 min at 95 °C with stirring, after which, an excess of 0.04 M ascorbic acid was added to the vial (500 μL). The solutions were then heated for an additional 30 min at 95 °C with stirring. A color change was observed over the first few minutes from lighter to darker brown (this change was more obvious with the vials containing more Rh precursor solution). The solutions were removed from heat and then transferred to a 50 mL centrifuge tube to be centrifuged for 15 min at 7000 rpm. The clear supernatant was decanted and discarded to yield a concentrated solution of Pd−Rh NCs, which were washed prior to characterization and loading on the catalyst support.

Particle Cleaning and Electrode Preparation. Eight syntheses of Pd@Rh 30 nm cube or 60 nm octahedra particles were centrifuged, combined, and redispersed to 10 mL. Before loading the particles onto the electrode, the particles were thoroughly cleaned to remove the chemicals on the surface. Using modification of a procedure from the literature,[58] a layer of Cu_2O was first coated onto the surface of the NCs and then was completely removed by etching and washing. The activity of electrochemical catalysis increased dramatically after these steps. The results suggest that the Cu_2O coating displaces the surface chemicals after the coating and is etched away to give a cleaner metal surface. Deionized water (95 mL), concentrated particle solution (1 mL), 1 M NaOH (2.5 mL), 0.2 M NH_2OH (6.5 mL), and 0.1 M $CuCl_2$ (0.05 mL) were combined and left to sit for 30 min at room temperature. The solution was centrifuged, the supernatant was discarded, and the concentrated particle solution was redispersed in 5 mL of methanol. The solution was centrifuged again, and the concentrated solution was dispersed in 5 mL of deionized water. The particles were left in water for 24 h, after which the solution was centrifuged and the supernatant was discarded. Five μL of cleaned, concentrated particle solution was deposited onto the previously alumina-polished surface of a glassy carbon working electrode (CH Instruments).

Electrochemical Measurements. A typical three-electrode system was used to perform the electrochemical experiments: a glassy carbon working electrode with deposited particles, a saturated calomel reference electrode (CH Instruments), and a platinum auxiliary electrode (CH Instruments) were connected to a potentiostat system (BioLogic VSP). The electrode was put into a three-neck flask containing 0.5 M H_2SO_4 that had been previously bubbled with nitrogen gas (to purge the electrolyte of oxygen gas). Fifty cycles of blank scans were carried out at a scan rate of 100 mV/s, scanning from −0.2 to 1.0 V. CO-stripping experiments were performed after the blank scans: The electrode was put into a three-neck flask containing 0.1 M $HClO_4$ and carbon monoxide was bubbled into the flask for more than 30 min. The electrode was then transferred to a flask containing 0.1 M $HClO_4$ that had been previously bubbled with nitrogen gas. Cyclic voltammetry was carried out at a scan rate of 10 mV/s, scanning from 0 to 1.0 V. The electrochemically active surface area (ECSA) of the electrode was determined by measuring the charge in the CO-stripping peak of the voltammogram. Formic acid oxidation experiments were performed in a flask which was 0.5 M in $HClO_4$ and 0.5 M in HCOOH that had been previously bubbled with nitrogen gas. Cyclic voltammetry was carried out at a scan rate of 100 mV/s, scanning from −0.2 to 1.2 V. The current density for formic acid oxidation was normalized by the ECSA determined by CO stripping.

■ ASSOCIATED CONTENT

Ⓢ Supporting Information

Additional data regarding the synthesis and characterization of substrates and bimetallic NCs, including STEM, EDX, XRD, SEM, TEM, HRTEM, UV−vis spectroscopy, photos, crystal models, and experiments which support the work. This material is available free of charge via the Internet at http://pubs.acs.org.

■ AUTHOR INFORMATION

Corresponding Author

frank.tsung@bc.edu

Notes

The authors declare no competing financial interest.

■ ACKNOWLEDGMENTS

Thanks to Boston College for funding the research. Thanks to M. Sheehan, J. Zhuang, and L. Lamontagne for supplying materials. Special thanks to Dr. D. Z. Wang for the help of instrumentation. Thanks to Prof. D. W. Wang and the Wang group for valuable discussions and use of instrumentation. Thanks also for use of TEM instrumentation facilities at National Tsing Hua University in Taiwan. C.H.K. thanks National Science Council in Taiwan for offering the scholarship. We appreciate Dr. Shaul Aloni and Virginia Altoe's help with STEM measurement. The work at the Molecular Foundry was supported by the Office of Science, Office of Basic Energy Sciences, of the U.S. Department of Energy under contract no. DE-AC02-05CH11231. C.N.B. thanks Northeast Section of the ACS (NESACS) for offering Norris Richards Undergraduate Summer Research Scholarship.

■ REFERENCES

(1) Fan, F.-R.; Liu, D.-Y.; Wu, Y.-F.; Duan, S.; Xie, Z.-X.; Jiang, Z.-Y.; Tian, Z.-Q. *J. Am. Chem. Soc.* **2008**, *130*, 6949.
(2) Yamada, Y.; Tsung, C.-K.; Huang, W.; Huo, Z.; Habas, S. E.; Soejima, T.; Aliaga, C. E.; Somorjai, G. A.; Yang, P. *Nat. Chem.* **2011**, *3*, 372.
(3) Alayoglu, S.; Nilekar, A. U.; Mavrikakis, M.; Eichhorn, B. *Nat. Mater.* **2008**, *7*, 333.
(4) Nilsson, A.; Pettersson, L. G. M.; Hammer, B.; Bligaard, T.; Christensen, C. H.; Nørskov, J. K. *Catal. Lett.* **2005**, *100*, 111.
(5) Gandhi, H. S.; Graham, G. W.; McCabe, R. W. *J. Catal.* **2003**, *216*, 433.
(6) Zhang, Y.; Grass, M. E.; Huang, W.; Somorjai, G. A. *Langmuir* **2010**, *26*, 16463.
(7) Zhang, Y.; Janyasupab, M.; Liu, C.-W.; Li, X.; Xu, J.; Liu, C.-C. *Adv. Funct. Mater.* **2012**, *22*, 3570.
(8) Yuan, Y.; Yan, N.; Dyson, P. J. *ACS Catalysis* **2012**, *2*, 1057.
(9) Breit, B. 2007, *24*, 145.
(10) Cappillino, P. J.; Sugar, J. D.; Hekmaty, M. A.; Jacobs, B. W.; Stavila, V.; Kotula, P. G.; Chames, J. M.; Yang, N. Y.; Robinson, D. B. *J. Mater. Chem.* **2012**, *22*, 14013.
(11) Bergamaski, K.; Gonzalez, E. R.; Nart, F. C. *Electrochim. Acta* **2008**, *53*, 4396.
(12) Sathe, B. R.; Balan, B. K.; Pillai, V. K. *Energy Environ. Sci.* **2011**, *4*, 1029.
(13) Jacinto, M. J.; Kiyohara, P. K.; Masunaga, S. H.; Jardim, R. F.; Rossi, L. M. *Appl. Catal., A* **2008**, *338*, 52.
(14) Gustafson, J.; Westerström, R.; Mikkelsen, A.; Torrelles, X.; Balmes, O.; Bovet, N.; Andersen, J. N.; Baddeley, C. J.; Lundgren, E. *Phys. Rev. B* **2008**, *78*, 045423.
(15) Park, K.-W.; Han, D.-S.; Sung, Y.-E. *J. Power Sources* **2006**, *163*, 82.
(16) Sathe, B. R.; Shinde, D. B.; Pillai, V. K. *J. Phys. Chem. C* **2009**, *113*, 9616.
(17) Suo, Y.; Hsing, I. M. *J. Power Sources* **2011**, *196*, 7945.
(18) Yuan, Q.; Zhou, Z.; Zhuang, J.; Wang, X. *Inorg. Chem.* **2010**, *49*, 5515.
(19) Zhang, Y.; Grass, M. E.; Kuhn, J. N.; Tao, F.; Habas, S. E.; Huang, W.; Yang, P.; Somorjai, G. A. *J. Am. Chem. Soc.* **2008**, *130*, 5868.
(20) Friebel, D.; Viswanathan, V.; Miller, D. J.; Anniyev, T.; Ogasawara, H.; Larsen, A. H.; O'Grady, C. P.; Nørskov, J. K.; Nilsson, A. *J. Am. Chem. Soc.* **2012**, *134*, 9664.

(21) Adleman, J. R.; Boyd, D. A.; Goodwin, D. G.; Psaltis, D. *Nano Lett.* **2009**, *9*, 4417.
(22) Niu, W.; Zhang, L.; Xu, G. *ACS Nano* **2010**, *4*, 1987.
(23) Chen, M.; Wu, B.; Yang, J.; Zheng, N. *Adv. Mater.* **2012**, *24*, 862.
(24) Zhang, H.; Li, W.; Jin, M.; Zeng, J.; Yu, T.; Yang, D.; Xia, Y. *Nano Lett.* **2010**, *11*, 898.
(25) Zhang, H.; Xia, X.; Li, W.; Zeng, J.; Dai, Y.; Yang, D.; Xia, Y. *Angew. Chem., Int. Ed.* **2010**, *49*, 5296.
(26) Long, N. V.; Chien, N. D.; Hirata, H.; Matsubara, T.; Ohtaki, M.; Nogami, M. *J. Cryst. Growth* **2011**, *320*, 78.
(27) Bi, Y.; Lu, G. *Chem. Commun.* **2008**, 6402.
(28) Zhang, Y.; Grass, M. E.; Habas, S. E.; Tao, F.; Zhang, T.; Yang, P.; Somorjai, G. A. *J. Phys. Chem. C* **2007**, *111*, 12243.
(29) Humphrey, S. M.; Grass, M. E.; Habas, S. E.; Niesz, K.; Somorjai, G. A.; Tilley, T. D. *Nano Lett.* **2007**, *7*, 785.
(30) Biacchi, A. J.; Schaak, R. E. *ACS Nano* **2011**, *5*, 8089.
(31) Ewers, T. D.; Sra, A. K.; Norris, B. C.; Cable, R. E.; Cheng, C.-H.; Shantz, D. F.; Schaak, R. E. *Chem. Mater.* **2005**, *17*, 514.
(32) Kobayashi, H.; Lim, B.; Wang, J.; Camargo, P. H. C.; Yu, T.; Kim, M. J.; Xia, Y. *Chem. Phys. Lett.* **2010**, *494*, 249.
(33) Lim, B.; Jiang, M.; Camargo, P. H. C.; Cho, E. C.; Tao, J.; Lu, X.; Zhu, Y.; Xia, Y. *Science* **2009**, *324*, 1302.
(34) Habas, S. E.; Lee, H.; Radmilovic, V.; Somorjai, G. A.; Yang, P. *Nat. Mater.* **2007**, *6*, 692.
(35) Jiang, M.; Lim, B.; Tao, J.; Camargo, P. H. C.; Ma, C.; Zhu, Y.; Xia, Y. *Nanoscale* **2010**, *2*, 2406.
(36) Alayoglu, S.; Eichhorn, B. *J. Am. Chem. Soc.* **2008**, *130*, 17479.
(37) Li, Y.; Liu, Q.; Shen, W. *Dalton Trans.* **2011**, *40*, 5811.
(38) Valden, M.; Lai, X.; Goodman, D. W. *Science* **1998**, *281*, 1647.
(39) Zhou, X.; Xu, W.; Liu, G.; Panda, D.; Chen, P. *J. Am. Chem. Soc.* **2009**, *132*, 138.
(40) Chantry, R. L.; Siriwatcharapiboon, W.; Horswell, S. L.; Logsdail, A. J.; Johnston, R. L.; Li, Z. Y. *J. Phys. Chem. C* **2012**, *116*, 10312.
(41) González, E.; Arbiol, J.; Puntes, V. F. *Science* **2011**, *334*, 1377.
(42) Venables, J. A.; Spiller, G. D. T.; Hanbucken, M. *Rep. Prog. Phys.* **1984**, *47*, 399.
(43) Koch, R. *J. Phys.: Condens. Matter* **1994**, *6*, 9519.
(44) Colombi Ciacchi, L.; Pompe, W.; De Vita, A. *J. Phys. Chem. B* **2003**, *107*, 1755.
(45) Nolte, P.; Stierle, A.; Jin-Phillipp, N. Y.; Kasper, N.; Schulli, T. U.; Dosch, H. *Science* **2008**, *321*, 1654.
(46) Koper, M. T. M. *Nanoscale* **2011**, *3*, 2054.
(47) Housmans, T. H. M.; Feliu, J. M.; Koper, M. T. M. *J. Electroanal. Chem.* **2004**, *572*, 79.
(48) Xu, Q.; Linke, U.; Bujak, R.; Wandlowski, T. *Electrochim. Acta* **2009**, *54*, 5509.
(49) Adić, R. R.; Tripković, A. V. J. *J. Electroanal. Chem. Interfacial Electrochem.* **1979**, *99*, 43.
(50) Rice, C.; Ha, S.; Masel, R. I.; Wieckowski, A. *J. Power Sources* **2003**, *115*, 229.
(51) Grozovski, V.; Solla-Gullχón, J.; Climent, V. c.; Herrero, E.; Feliu, J. M. *J. Phys. Chem. C* **2010**, *114*, 13802.
(52) Serpell, C. J.; Cookson, J.; Ozkaya, D.; Beer, P. D. *Nat. Chem.* **2011**, *3*, 478.
(53) Fan, N.; Yang, Y.; Wang, W.; Zhang, L.; Chen, W.; Zou, C.; Huang, S. *ACS Nano* **2012**, *6*, 4072.
(54) Wang, D.; Li, Y. *J. Am. Chem. Soc.* **2010**, *132*, 6280.
(55) Chen, H.; Wang, F.; Li, K.; Woo, K. C.; Wang, J.; Li, Q.; Sun, L.-D.; Zhang, X.; Lin, H.-Q.; Yan, C.-H. *ACS Nano* **2012**, *6*, 7162.
(56) Chang, C.-C.; Wu, H.-L.; Kuo, C.-H.; Huang, M. H. *Chem. Mater.* **2008**, *20*, 7570.
(57) Wu, H.-L.; Kuo, C.-H.; Huang, M. H. *Langmuir* **2010**, *26*, 12307.
(58) Kuo, C.-H.; Hua, T.-E.; Huang, M. H. *J. Am. Chem. Soc.* **2009**, *131*, 17871.